


Aging-induced dynamics for statically indeterminate systems

Jr-Jiun Lin, Chi-Chun Cheng, Yu-Chuan Cheng, and Tzay-Ming Hong*

Department of Physics, National Tsing Hua University, Hsinchu 30013, Taiwan, Republic of China (Received 29 December 2020; revised 10 June 2021; accepted 18 October 2021; published 9 November 2021)

Statically indeterminate systems are experimentally demonstrated to be in fact dynamical. Take the classic problems of a beam with three supporting points, granules in a silo, and a ladder leaning against a wall, for instance; their reaction forces are found to vary logarithmically for over 10^4 s with an increment or decrement of more than 10%. This seemingly contradictory mixture of dynamics for a static system is shown to derive from the evolution of microcontact area with the ground and/or wall due to the aging effect.

DOI: [10.1103/PhysRevE.104.054902](https://doi.org/10.1103/PhysRevE.104.054902)**I. INTRODUCTION**

Statically indeterminate systems are frequently encountered by architects, engineers, and physicists, such as a chair or a beam with more than three or two legs or supporting points, the weight of granules in a silo, and a ladder leaning against the wall, as depicted schematically in Figs. 1(a)–1(c). The reaction forces outnumber the equilibrium equations in these systems and, therefore, are insufficient to be uniquely determined. Physically, this implies that they are prone to small perturbations because there are an infinite number of solutions.

For the sake of illustration, we shall first concentrate on the ladder-wall problem known to all students learning statics [1] as well as a practical case concerning industrial safety [2,3] and report an unanticipated dynamical property that has eluded the scrutiny of scientists for so many years. Consider the beam in Fig. 1(c). The friction and normal forces are denoted by $f_{1,2}$ and $N_{1,2}$, where subscripts 1 and 2 refer to the reaction from the floor and wall. At equilibrium, the equations balancing planar forces and torques can be written as:

$$\begin{aligned} N_2 &= f_1 \\ N_1 + f_2 &= W \\ \frac{W}{2}(L \cos \theta - d \sin \theta) &= f_2 L \cos \theta + N_2 L \sin \theta, \end{aligned} \quad (1)$$

where W , L , and d denotes the weight, length, and width of the beam. Clearly these three equations are insufficient to uniquely determine the four unknown reactions.

Various textbooks and researchers have considered the problem [4,5], but there is no consensus so far. For instance, Mendelson [6–9] argued in 1994 that the correct limiting condition is that the friction force at the top of ladder is equal to the maximum static friction. This was disputed by González and Gratton [10] two years later, who proposed that the missing condition lies in analyzing flexion. Dissatisfied with both assumptions, we decided to verify their validity and

come up with a less ad hoc theory. But, as will be delineated later, more mysteries were unfolded, mainly an unexpected dynamical behavior for this static setup [11].

II. EXPERIMENTAL SETUP AND METHODOLOGY

To probe the nature of the ladder-wall system, three separate observations, namely the (a) photoelastic (PE) response, (b) time evolution of forces, and (c) real contact area were analyzed. The setup for these three observables will be specified explicitly later. In our experiments, the indeterminacy in Eq. (1) is resolved by measuring f_1 . As shown schematically in Fig. 1(c), the beam is placed on a movable floor piece where all friction is eliminated by the rollers underneath [12], and f_1 comes solely from the fixed horizontal force sensor (Futek LRF 400). The sensor is placed on a micrometer, effectively allowing us to fine-tune the geometry and initial conditions of the setup. Experiments are all conducted on an optical table with a rectangular aluminum beam of $L = 10$ cm, $d = 4$ cm, and $W = 475$ gw. In practice, measurements of f_1 are largely influenced by initial conditions and ambient noise. To eliminate these factors, the beam is kept several millimeters away from the wall before each trial with an automated electromagnet. By shutting down the electromagnet, the beam is gently dropped onto its leaning position in a controlled and reproducible fashion at the designated angle. Furthermore, the entire setup is put in a large box to shield from wind, while temperature is conditioned at $20 \pm 1^\circ\text{C}$ and humidity at 50 to 55%.

A. Photoelastic response

The wide range of solutions allowed by the system can be illustrated by attaching a piece of photoelastic material, PSM-4 by Vishay Instruments, onto the rigid wall [13,14]. By imposing a minute displacement $\epsilon \approx 0.2$ mm on the floor piece via adjusting the micrometer so that the change in θ is negligible, redistribution of the local stress on the PSM-4 can be observed, as well as a substantial variation in the measured forces, shown in Figs. 1(d)–1(g)

*ming@phys.nthu.edu.tw

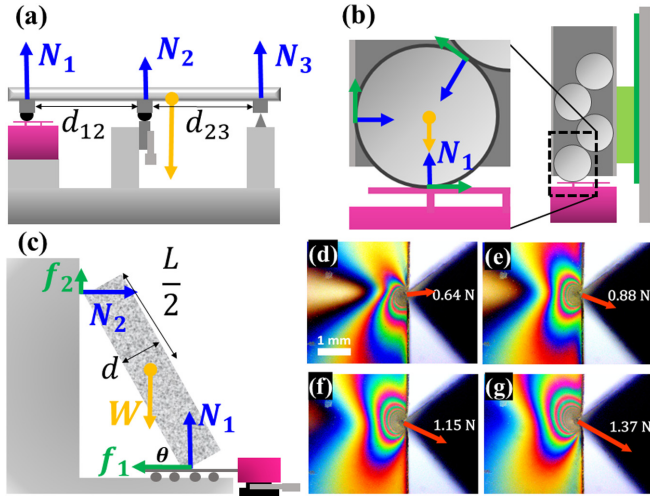


FIG. 1. Schematics of the experimental setup and free body diagram for (a) a beam with three supports, (b) a narrow granular silo, and (c) the ladder-wall system. Normal and frictional forces are represented by blue and green arrows, while weight in yellow. Box in magenta represents the force sensor. [(d)–(g)] Close-up photoelastic images at the contact point between the ladder and wall. Starting from (d), the micrometer drives forward a distance of $\epsilon \approx 0.2$ mm before the next photo is taken. Force vectors in red arrow are then calculated from the corresponding reading of the force sensor.

Contrary to conventional wisdom in statics, it came to our attention that the stress distribution is in fact dynamical. A series of photoelastic photos were taken at different times with the PE setup. To facilitate contrast, the images at subsequent $t > 0$ are turned into gray scale and subtracted from that at $t = 0$. The illuminated area corresponds to where fringes have expanded into. Figures 2(a)–2(c) show that the expansion is

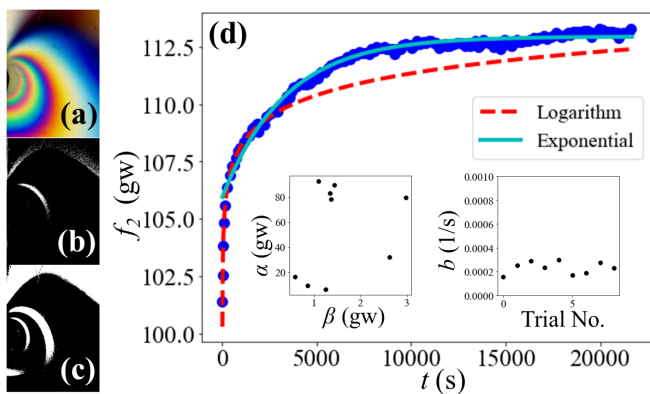


FIG. 2. (a) Side view of local photoelastic fringes on PSM-4 attached on the wall at $t = 0$. [(b) and (c)] Differential image of the same view for contrast at $t = 10$ and 500 s. (d) Typical data of f_2 in the main setup at $\theta = \pi/4$. For $t \leq 3 \times 10^3$ s, the data can be fit by the dashed line, $\alpha + \beta \ln t$ with $\alpha = 105.1$ gw and $\beta = 1.367$ gw. But if we expand t to 2×10^4 s, then $a \exp(-bt) + c$ with $a = -7.000$ gw, $b = 2.91 \times 10^{-4}$ 1/s, and $c = 112.953$ gw becomes a better fit (solid line). The left inset shows that the values of α , β fluctuate with different tries and there is no obvious correlation. In contrast, $b \approx (2.32 \pm 0.52) \times 10^{-4}$ in the right inset.

considerable, suggesting a comparable rate of increase for stress in the vicinity of contact points.

B. Main setup and time evolution of forces

To rule out possible viscoelastic effects from the PSM-4, the wall was replaced by a fixed large aluminum block, with an #80 aluminium oxide abrasive paper of surface roughness $R_a = 1.8 \mu\text{m}$ attached to the surface. This renders a larger static friction coefficient for the benefit of later experiments. In addition, we attached a hard PVC edge guard by 3M with Young’s modulus ≈ 2 GPa to the contact edge of the aluminum beam against the wall. The edge guard avoids unwanted effects from the sharp edge of the aluminum beam and is regularly renewed after each trial along with the abrasive paper. We have checked the robustness of our conclusions by (1) removing the edge guard and sand paper from the beam-wall contact, (2) blunting the sharp edge of beam to increase its contact area with the wall, and (3) testing on other materials (i.e., acrylic, stainless steel, and wooden beams) and shapes (such as whiteboard pen and sharpened pencil.)

Unexpectedly, experiments conducted with the main setup described above shows the reading to drop monotonically for up to 2×10^4 s. Such a trend reflects a 10% increase in f_2 , as shown in Fig. 2(d). To check whether the beam is subject to any mesoscopic slippage, a standard optical lever experiment with a mirror on the back of the beam is carried out. It is estimated that such variation in the reaction forces would correspond to roughly 10^{-3} rad in θ for $\theta \approx \pi/4$, yet no variation of this magnitude was observed. For the benefit of later discussions, we convert the f_1 data to f_2 in Fig. 2(d) that can be nicely fit by $\alpha + \beta \ln t$, characteristic of an aging effect [15–17]. Deviations eventually becomes evident as the data approach a flat plateau after roughly 10^4 s, where $a \exp(-bt) + c$ becomes a better fit.

A logarithmic growth in static friction coefficient μ , known as frictional aging, has been observed for various materials including metals [18,19], rocks [20,21], and glassy polymers [22–26]. One may falsely think that the observed time evolution of f_2 stems from the aging of μ_2 . This would amount to assume that the contact point with the wall is constantly at its Coulomb threshold, i.e., on the verge of slipping at all angles. This proposal is rejected by the ratio f_2/N_2 calculated from data in Fig. 2(d), which never reaches the measured μ_2 in its growth until several hours into the trial, as shown in Appendix B.

C. Theoretic analysis of static conditions

In Fig. 2(d), we observed that the logarithmic fitting fails after 2×10^4 s. This hints at the existence of an intrinsic value for the reaction forces that is static and presumably hidden in Eq. (1). We were thus motivated to revisit the unsettled problem of what the missing condition to Eq. (1) is. In the following we shall propose that simplification and analytic solutions for $f_{1,2}(\mu_2, \theta)$ are possible in the case of small deformations. It is heuristic to note that the axial “squeezing” force on the beam can take on arbitrary value as long as Eq. (1) is satisfied, while the extent of bending is uniquely determined by the weight. Therefore, minimizing the compressing force

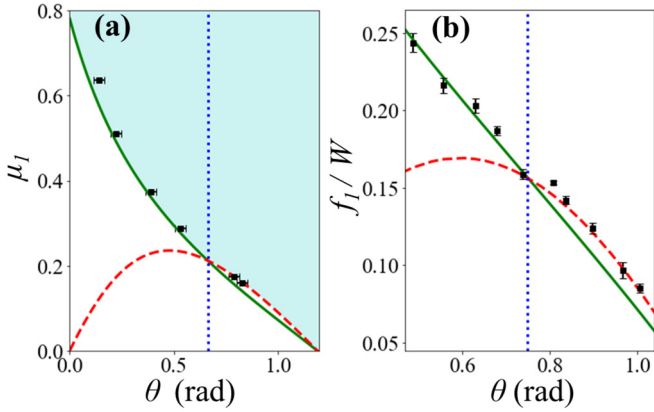


FIG. 3. (a) Phase diagram for μ_1 vs. θ with $\mu_2 = 1.07$. Consistent with the experimental data points, the beam will slip if μ_1 falls below the solid line from Eqs. (2) when $\theta \leq \theta_c = \cot^{-1}(\mu_2)$ marked by the vertical dotted line. Meanwhile, for $\theta \geq \theta_c$ instability is triggered when μ_1 is below the dashed line from Eq. (3). (b) Value of f_1 is normalized by W and plotted against θ with $\mu_1 = 0.51$ and $\mu_2 = 1.07$. The solid and dashed lines represent solutions determined by Eqs. (4) and (5), respectively.

from the wall, $N_2 \cos \theta - f_2 \sin \theta$, can fill in as the fourth condition missing from Eq. (1), and the Young's modulus does not enter the equation.

However, there are two caveats. First, $N_2 \cos \theta - f_2 \sin \theta$ can never be negative. Second, the friction $f_{1,2}$ should never exceed $\mu_{1,2}N_{1,2}$ where $\mu_{1,2}$ denotes the static friction coefficient from the floor and wall. By imposing these two conditions, we can obtain the boundary beyond which no solution can exist:

$$\mu_1 = \frac{1 - \frac{d}{L} \tan \theta}{\mu_2(1 + \frac{d}{L} \tan \theta) + 2 \tan \theta} \quad (2)$$

and

$$\mu_1 = \frac{1 - \frac{d}{L} \tan \theta}{\cot \theta(1 + \frac{d}{L} \tan \theta) + 2 \tan \theta}. \quad (3)$$

Detailed derivations can be found in Appendix C. Equations (2) and (3) indicate that these two phase boundaries are each determined by $\mu_2 N_2 = f_2$ and $N_2 \cos \theta - f_2 \sin \theta = 0$, which is represented in Fig. 3(a) by the green solid and red dashed lines, respectively. The beam will slip when its angle falls below either line.

To properly discern these two phase boundaries in experiments, a large μ_2 is required, which is why the abrasive paper was added. The predictions of Eqs. (2) and (3) are then examined by experiments in the main setup, where different materials are attached to the floor piece in order to vary μ_1 as the controlled parameter. A series of drops by the electromagnet with decreasing θ are performed until the beam slips, which indicates the boundary. The data points in Fig. 3(a) were obtained under this protocol, offering vindication to Eqs. (2) and (3).

Note that Eq. (2) is equivalent to that derived by previous studies [7,9] where f_2 is supposed to be at its maximum value. But instead of just a single phase boundary, we argue that the phase boundary at $\theta \geq \theta_c$ is governed by Eq. (3) instead of (2).

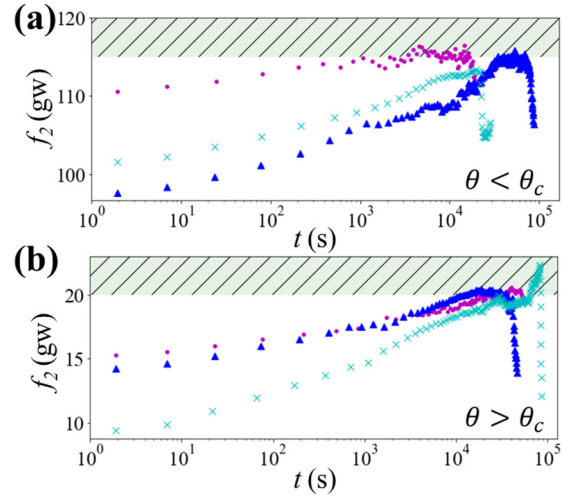


FIG. 4. (a) Evolution of f_2 for three distinct trials with identical setup and conditions is plotted against $\log t$ with $\theta = 0.54$ rad. Shaded bar indicated the maximum value of f_2 beyond which $f_2 \leq \mu_2 N_2$ will be violated. However, note that μ_2 may increase slightly with t [16]. Data points far beyond the steep drop are not shown for clarity. (b) Three trials for $\theta = 0.96$ rad. Shaded bar indicates the forbidden regime where $N_2 \cos \theta - f_2 \sin \theta \leq 0$.

A heuristic way to understand this is that the beam is never in danger of slipping at large θ and, therefore, f_2 never reaches the Coulomb threshold $\mu_2 N_2$.

Furthermore, in determining the magnitude of $f_{1,2}$ and $N_{1,2}$, the beam prefers to allocate its weight to f_2 as much as possible so that $N_2 \cos \theta - f_2 \sin \theta$ can assume a smaller value to minimize the axial compression energy. Consequently, by requiring the equality in Eqs. (2) and (3) to hold separately, the system is no longer indeterminate and explicit solutions can be acquired as:

$$f_1 = W \left[-\frac{d}{2L} + \frac{\cot \theta}{2} - \frac{\mu_2(\cot \theta - d/L)}{4(\mu_2 + \tan \theta)} \right] \quad (4)$$

for $\theta \leq \theta_c$ and

$$f_1 = W \left[-\frac{d}{2L} + \frac{\cot \theta}{4} - \frac{\sin 2\theta}{8} \left(1 - \frac{d}{L} \right) \right] \quad (5)$$

for $\theta \geq \theta_c$.

This prediction is put to the test in the main setup where $\mu_1 = 0.51$ and $\mu_2 = 1.07$, while data are collected at roughly 10^3 s. The match between experimental results and theory in Fig. 3(b) offers convincing evidence that minimizing the compression energy indeed plays a decisive role. But how to incorporate the static value predicted by Eqs. (4) and (5) into the dynamic evolution we observed in Fig. 2?

It turns out that these two equations, set respectively by $f_2 = \mu_2 N_2$ and $N_2 \cos \theta - f_2 \sin \theta = 0$ at small and large θ , define the upper cutoff in Figs. 4(a) and 4(b) beyond which the $\ln t$ fitting fails at $t \approx 10^4$ s. Although the initial value of f_2 varies with different trials, they all observe the same logarithmic growth at short time and level off before their maximum value is reached. In addition, the aging of μ could not have been the sole root source of such dynamics, since in Figs. 4(a) and 4(b) similar dynamics in f_2 is observed for θ

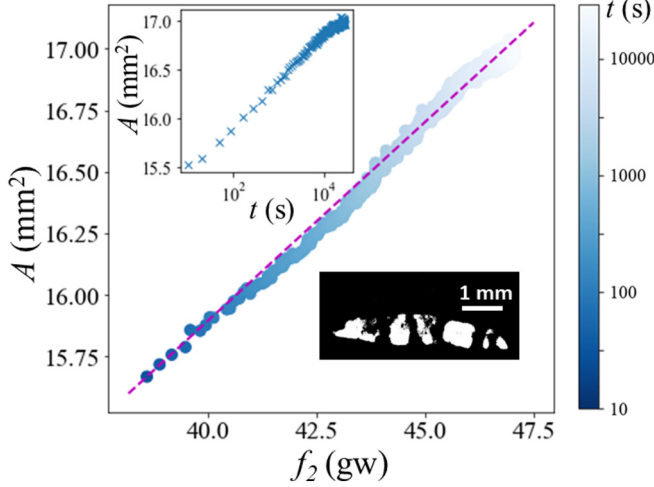


FIG. 5. A vs f_2 is plotted over roughly 10 hours for $\theta = \pi/4$. The linear red dashed line is a guide for the eye. Upper inset shows the logarithmic growth of $A(t)$ in the same trial, consistent with previous studies on aging effect [24,28,29]. Lower inset shows binarized images of the rough contact against the glass wall.

smaller and greater than θ_c . In the latter case, the Coulomb threshold is never reached, and thus μ_2 and its aging are irrelevant.

D. Measurement of real contact area

To establish a positive correlation between aging and the dynamics in Fig. 2, we decide to measure another aging-related quantity, real contact area A , in tandem with f_2 . It is known that the growth in μ stems from the creep of asperities between the two contact surfaces, resulting in an observable increase of A which is generally only a small fraction of the apparent surface area [15–17]. Such contacts between asperities are recognized as proxy for frictional force [15,24,27] and can be directly observed to the micrometer scale via optical procedures [24,28,29].

We thus deployed the real contact area setup by leaning the beam against a smooth glass with a thin silicone-rubber elastomer padding attached to its end. Light from a LED source is injected from the side of the glass such that it is totally internal reflected except at the contact points where it is scattered and effectively illuminates the area of real contacts to the scale of several microns. The scattered light is captured by the charge-coupled device camera on the opposite side of the glass, whose intensity is then binarized for quantitative analysis, as demonstrated by Fig. 5(a). One pixel corresponds to $10 \mu\text{m} \times 10 \mu\text{m}$. Results in Fig. 5(a) show that within the time range of 10^4 s, f_2 and A maintain a steady linear relation. This confirms the aging of contact area follows an identical time evolution as the increasing f_2 .

In a fully determined system, static friction emerges only as a reaction upon external shear, and frictional aging refers only to the logarithmic increase of μ . In contrast, a statically indeterminate system allows for a broad range of possible solutions, which opens the door for the aging of A to induce the time dependence for the reaction forces. Mathematically, this is made possible by the fact that each term in Eq. (1)

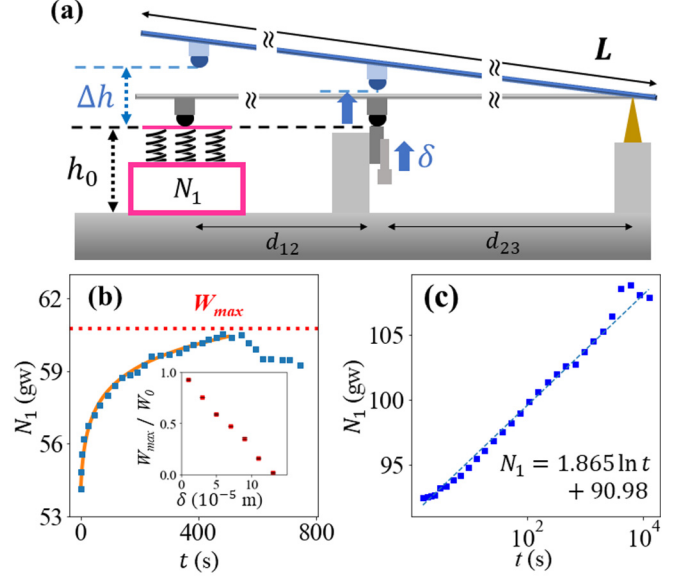


FIG. 6. (a) Schematics of the setup for a horizontal beam with three supports. (b) The normal force on the far left, N_1 , is plotted against time. The orange line denotes a logarithmic fitting line of $N_1 = 54.15 + 1.363 \ln t$. Inset shows that the upper threshold of N_1 decreases linearly with the magnitude of ascent, δ , in the middle support. (c) The normal force, defined in Fig. 1(b) for the granular silo experiment with 11 beads, is plotted over time. Straight dashed line is the logarithmic fitting function to the first 10^4 s of data.

in reality involves an integration over the real contact area between the ladder and the wall and floor. Increasing contact points is like adding more legs to a chair, which naturally will redistribute the weight and vary the normal force on each existing leg. What remains elusive to us is why $f_2(t)$ ends up obeying the same time dependence as $A(t)$ in Fig. 5.

III. MORE INDETERMINATE SYSTEMS

To demonstrate that our conclusions are not limited to the particular geometry of the ladder-wall setup, we will move on to report similar findings in other statically indeterminate systems, i.e., the horizontal beam with three supports and a narrow granular silo displayed in Figs. 1(a) and 1(b).

A. Beam with three supports

A long horizontal beam laying on three collinear supporting points also falls in the category of statically indeterminate systems. Given that all force vectors are coplanar, the two equilibrium equations cannot uniquely determine the three normal forces supporting the weight of the beam illustrated in Fig. 1(a).

Experiments are performed with a thin aluminum beam of length 105 cm, $d_{12} = 19.9$ cm, and $d_{23} = 45.5$ cm, shown schematically in Fig. 6(a). A sharp brass blade on the right serves as the pivot point, while steel beads of diameter $2r = 14$ mm are fixed in aluminum adaptors as the other two support points. The normal force N_1 is measured with an electronic scale (T-Scale NB-1500) under the leftmost support. Care is taken to ensure that there is no horizontal force. Before

the start of each trial, the middle support is set at a height that equals h_0 , at which point it barely supports any weight, and N_1 remains steady at $W_0 = 300$ gw. Then, the middle support is slowly raised by a distance of $\delta \sim 10^{-5}$ m via a micrometer and introduces the third normal force. Meanwhile, the leftmost support remains in contact due to the elastic deformation of the electronic scale. This triggers the time evolution in Fig. 6(b), which can be nicely fit to a logarithmic growth function up to 500 s. Afterwards, N_1 drops, similar to Fig. 4 for the ladder-wall system.

The distinct turning point W_{\max} where the logarithmic growth ceases can be directly collected from the original data. For different values of δ , we observe a linear decrease in W_{\max}/W_0 up until $\delta = 14 \times 10^{-5}$ m when N_1 equals zero entirely. This result can be derived by assuming that the beam remains straight which requires the compression strain on the three supports to obey a linear relation, $x_1 + x_3 = 2x_2$. In the presence of δ , this provides a third condition to uniquely determine the threshold value of normal forces,

$$N_1 + N_3 = 2\left(N_2 - YA\frac{\delta}{2r}\right), \quad (6)$$

where Y and A are Young's modulus and cross sectional area of the middle support.

B. Granular silo

Another system that we checked is the granular silo in Fig. 1(b). By measuring the force exerted by the granules on the bottom plate that is detached from the silo [30], we again found the logarithmic relaxation for 10^4 s. Experimentally, an aluminum tube of diameter $2R = 26$ mm is filled with identical steel beads of diameter $2r = 14$ mm. The inner surface of the tube is covered by sand paper in order to maximize the friction. The bottom of the tube is open and placed slightly above an electronic scale with a gap of 5 mm before each measurement. After adding the beads, the tube is slowly pulled up a distance of 1 mm to fully "mobilize" the friction at contact points with the wall [31,32] to ensure the frictional force always points upwards for different trials. The normal force N_1 is then measured by the electronic scale placed below. The results shown in Fig. 6(c) again exhibits a logarithmic relaxation that lasts for around 10^4 s, during which the weight increases by more than 10% of the total weight for 11 beads.

This seems to differ from the ladder-wall case where the aging friction acts to decrease the compression energy and cause the observed weight N_1 to decrease. We note that relaxation process of *decreasing* weight for up to 100 s has been observed in Ref. [31], where the weight is measured by an electronic scale on a translation stage descending in steps. Similar experimental procedures have been conducted by Bratberg *et al.* [32] for a long narrow column where the relaxation is noticeable after the ascent of the scale but insignificant after the descent. These features may seem to disagree with our experiment at first glance. But we believe they are artifacts due to the higher pull-up velocity we chose, about two orders of magnitude larger than that of Bratberg *et al.* This gives the beads not enough time to

equilibrate during the pulling process. In addition, the high kinetic friction coefficient of sand paper further mobilizes the granular pile, resulting in considerable recompaction after the pulling.

The percentage of weight change is found to increase with the number of steel balls. Since this creates more contact points between beads and the wall, it renders the system more indeterminate by generating more unknown forces than the equilibrium conditions can afford to determine. Therefore, we infer that this unexpected dynamical relaxation is not only intrinsic to statically indeterminate systems, but also appears to be quantifiable by the degree of indeterminacy.

The implication is that relaxation dynamics can have a significant impact on the measured weight at the bottom, especially for experiments related to the Janssen effect where friction with the wall is crucial. Protocols for measurement and time-dependent behavior should thus be handled with care in future work.

IV. CONCLUSIONS AND DISCUSSION

In conclusion, we reported an unexpected dynamical behavior for the reaction forces in three statically indeterminate systems, i.e., a ladder leaning against the wall, a beam with three supports, and a granular silo. Experimental evidence and physical arguments are provided to correlate and link this time variance to that of real contact area due to aging. Furthermore, we are able to identify the origin of threshold, beyond which the monotonic increase for reaction forces is replaced by an irregular series of fluctuations and precipitous drop.

Since the logarithmic increase of real contact area due to aging is not limited to indeterminate systems, the distribution of normal forces under a brick or a house must also be dynamic if we analogize them to a desk with more than three miniaturized legs, although their sum is constrained by the fixed weight of the object. This generalization is demonstrated by the setup in Fig. 7(a) where a uniform load of 15 N is exerted to seven identical photoelastic PSM-4 pillars. Red and blue pixels in Fig. 7(b) shows the difference in pixels after 10^2 and 10^3 s, respectively. The dynamical fringes confirm that the distribution of normal forces shifts between different pillars with a slow relaxation time of several hundred seconds, qualitatively resembling the three-support-beam examined in Sec. III A.

With an increment up to 11% for the support force in Fig. 6(b), we dare not imagine the potential hazard this may pose to the safety of elevated highways and bridges. It will be interesting and important to study whether such a dynamical behavior might be suppressed by increasing the number of piers or unknown variables in mathematical term, namely the degree of indeterminacy. Although we have established a positive and causal relation between the dynamics of normal forces and that of real contact area, we stop short of proving that their time dependence is the same—at least before the normal force reaches its upper bound. Another challenge for future researchers is to decipher the irregular dynamics for both reaction forces and real contact area at long time and explain why their behavior ceases to be correlated. Preliminary

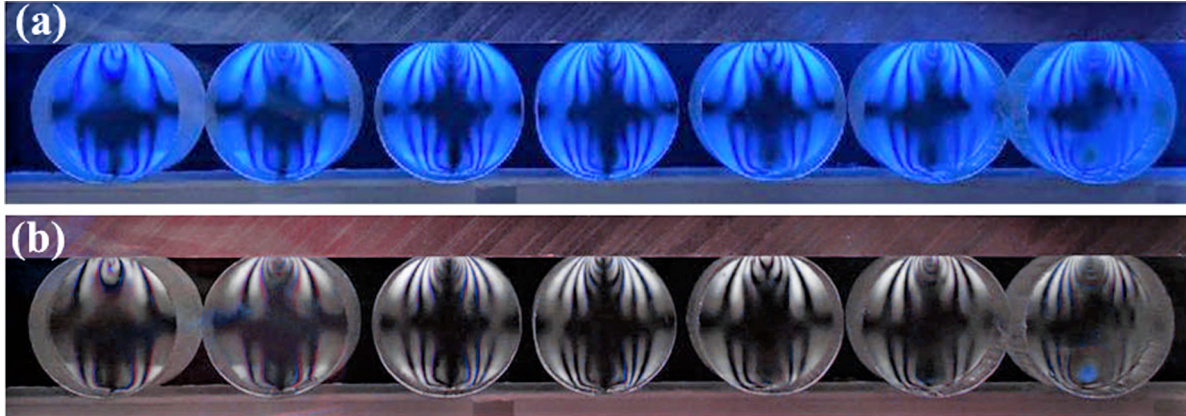


FIG. 7. Illuminated by polarized blue LED light, these seven PSM-4 pillars under a uniform load of 15 N exhibit distinct fringes that allow us to visualize the distribution of normal stress. Photo in (a) was taken at $t = 0$ when the load was added. (b) Red and blue pixels represent the differential image at $t = 100$ and $t = 1000$. For contrast, the intensity at $t = 0$ is juxtaposed in white pixels.

results showed that the fluctuations can last for weeks with amplitudes not diminished by time and the increase of weight. Whether they can eventually be identified as a new source of mechanical noise remains to be seen.

ACKNOWLEDGMENTS

We gratefully acknowledge technical assistance from Jih-Chiang Tsai, Wei-Shen Chen, Ke-Yang Hsiao, and Li-Min Wang; useful suggestions from Jih-Chiang Tsai; and financial support from the Ministry of Science and Technology in Taiwan under Grants No. 105-2112-M007-008-MY3 and No. 108-2112-M007-011-MY3.

APPENDIX A: CHARACTERIZATING FRICTION

The experimental confirmation of the phase diagram in the main text requires precise measurement of the μ value for various surfaces. Before each measurement, the edge guard placed on the bottom of the aluminum beam is cleaned by alcohol and dried. Thin patches of different material are then glued on the surface of an inclined aluminum board. A motor is used to slowly tilt the board, whose inclination angle is measured via an electronic level with uncertainty of $\pm 0.1^\circ$. The threshold angle θ_s when the beam starts to slip is recorded, and $\mu = \tan \theta_s$ can be calculated. Measurement for each material is repeated several times, while the edge guard is renewed every 10 trials to avoid wear. Results shown in Table I is used to plot the phase diagram in the main text.

TABLE I. Table of μ measured for various materials.

Material	μ
#80 Abrasive paper	1.070 ± 0.022
#120 Abrasive paper	0.637 ± 0.012
#200 Abrasive paper	0.509 ± 0.009
Copy paper	0.374 ± 0.008
Polypropylene film	0.176 ± 0.004
Polymethylmethacrylate	0.286 ± 0.005
Aluminum	0.277 ± 0.008

To double check the μ value obtained by the previous approach, we employed a pull test by a step motor and force gauge which measures the maximum static friction f_{max} under different loading weight W . Results in Fig. 8 show good agreement with Amonton’s friction law within $W \leq 3$ N, which is the magnitude of concern in our experiments. The fitted slope is consistent with that measured by the inclined plane. Furthermore, the inclination test is repeated with beams of different weight, which shows no significant effect on the resulting μ , as shown in the inset of Fig. 8.

APPENDIX B: COULOMB THRESHOLD

The logarithmic time dependence of f_2 observed in our experiments can be easily mistaken to be a direct consequence of the aging friction coefficient μ_2 , which is a well-studied topic. To rule out this wrong belief, a straightforward check can be done by calculating the ratio $f_2(t)/N_2(t)$. If the contact between the beam and wall is at the Coulomb threshold at all angles and moments, $f_2(t)/N_2(t)$ should accurately reflect $\mu(t)$ and its aging.

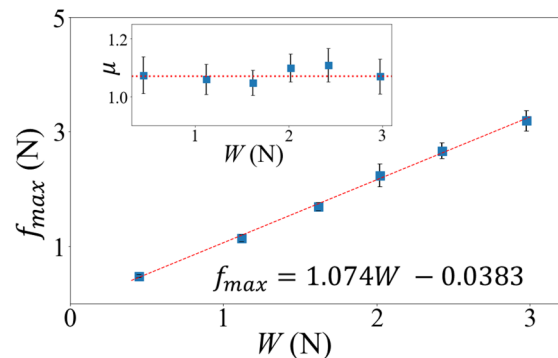


FIG. 8. The maximum static friction f_{max} between the edge guard and #80 abrasive paper under different weight W measured by a force gauge. Red dashed line is a linear fit with the shown expression. Inset: The μ value measured with the inclination test with different W . Red dotted line marks the total average.

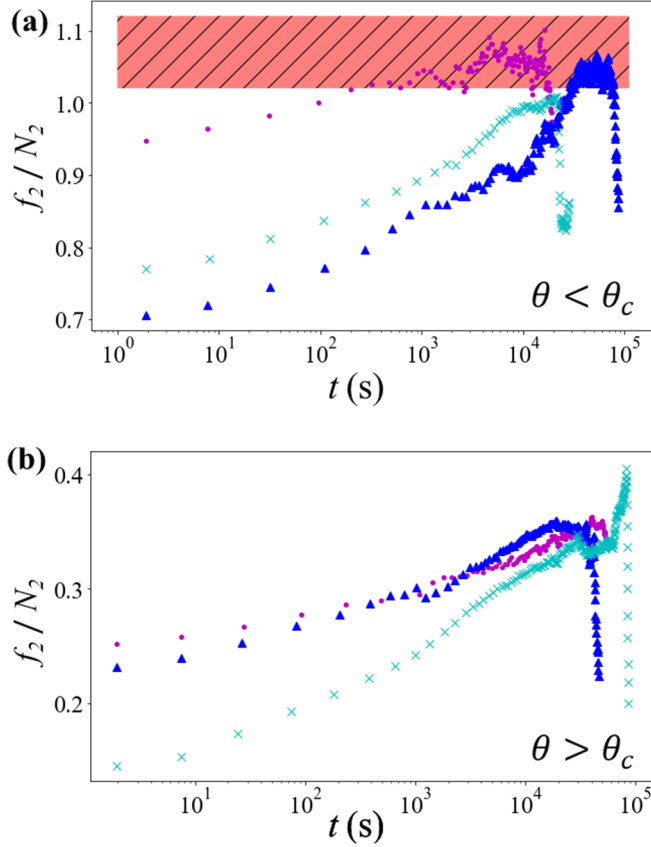


FIG. 9. (a) $f_2(t)/N_2(t)$ calculated from Fig. 4(a), and (b) from Fig. 4(b) with the same symbols for different set of data. Shaded bar in (a) represents the experimental value of μ_2 .

By use of Eq. (1), $N_2(t)$ can be readily obtained as:

$$N_2(t) = W \left[-\frac{d}{2L} + \frac{\cot \theta}{2} \right] - f_2(t) \cot \theta. \quad (\text{B1})$$

Data of $f_2(t)$ from Figs. 4(a) and 4(b) are then inserted to yield $f_2(t)/N_2(t)$, plotted in Fig. 9. It is clear that after 10^4 s, increment of $f_2(t)/N_2(t)$ generally falls around 0.2, which is considerably larger than 0.1 of an aging μ from frictional surfaces [16]. Furthermore, a large portion of the growth in Fig. 9(a) takes place at short times and far from the shaded bar that represents the measured μ_2 and its error bar in Fig. 8. As for the large-angle trials in Fig. 9(b), the maximum peak is less than half of μ_2 . This indicates that the contact at the wall is generally far from the Coulomb threshold, and the logarithmic growth in the first 10^4 s cannot be explained by the well-known aging of μ .

APPENDIX C: DECIDING PHASE BOUNDARIES

Balancing the torques requires that the perpendicular forces acting on both ends of the beam are equal and fixed. As a result, the extent of bending is uniquely determined by the weight. In contrast, the compression enjoys an additional degree of freedom. In other words, the the two axial “squeezing” force on the beam can take on arbitrary value as long as they are opposite and equal. We therefore propose the minimization of the compressing force from the wall,

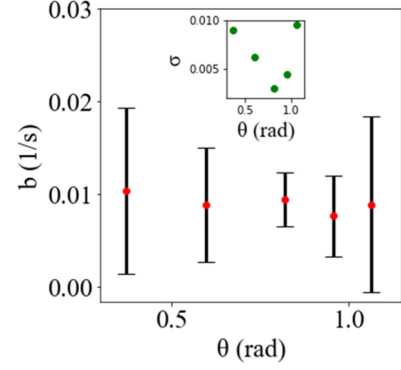


FIG. 10. The b value for the exponential fitting function, $a \ln(-bt) + c$, at different θ . Each dot represents the mean value from 10 trials. The range of θ is chosen to stride between the green solid line and the blue dotted vertical line in Fig. 3(a). The standard deviation σ in the inset is the largest at small and large θ .

$N_2 \cos \theta - f_2 \sin \theta$, as the fourth condition to solve the indeterminate problem.

The physical constraints, namely $N_2 \cos \theta - f_2 \sin \theta \geq 0$ and $f_{1,2} \leq \mu_{1,2} N_{1,2}$, can each be expressed solely in terms of N_1 :

$$N_1 \leq \frac{W}{2} \left(\cot \theta + \frac{d}{2L} \right) \equiv x_1(\theta, \mu_1), \quad (\text{C1})$$

$$N_1 \geq \frac{W \left(1 + \frac{\mu_2}{2} \cot \theta + \frac{\mu_2 d}{2L} \right)}{1 + \mu_2 \cot \theta} \equiv x_2(\theta, \mu_2), \quad (\text{C2})$$

$$N_1 \geq \frac{W \left(1 + \frac{1}{2} \cot^2 \theta + \frac{d}{2L} \cot \theta \right)}{\cot^2 \theta + 1} \equiv x_3(\theta), \quad (\text{C3})$$

where $x_{1,2}$ are constraints imposed by $\mu_{1,2}$, while x_3 comes from $N_2 \cos \theta - f_2 \sin \theta \geq 0$. We are concerned with the boundary beyond which no solution can exist. It is worth noting that only Eq. (C1) presents an upper bound. Hence, solutions of N_1 cease to exist if $x_1 < x_2$ or $x_1 < x_3$. It is then clear that $x_1 = x_2$ and $x_1 = x_3$ are the critical conditions that verge on instability, each of which can be rearranged into a neater form:

$$\mu_1 = \frac{1 - \frac{d}{L} \tan \theta}{\mu_2 \left(1 + \frac{d}{L} \tan \theta \right) + 2 \tan \theta} \quad (\text{C4})$$

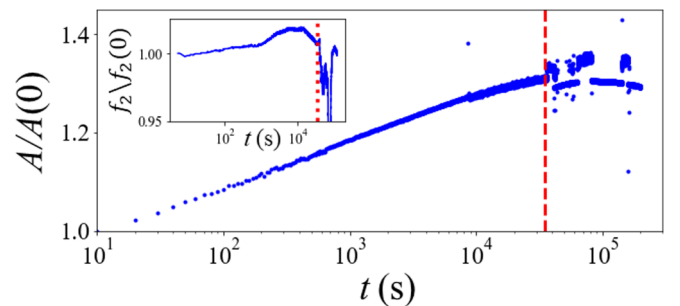


FIG. 11. As the measured f_2 drops spontaneously in the inset, A underwent noticeable fluctuation. The dashed vertical line marks and shows that the onset of these two phenomena coincide.

and

$$\mu_1 = \frac{1 - \frac{d}{L} \tan \theta}{\cot \theta \left(1 + \frac{d}{L} \tan \theta\right) + 2 \tan \theta}. \quad (\text{C5})$$

Equations (C4) and (C5) define the two phase boundaries presented in the main text.

APPENDIX D: FLUCTUATIONS FOR INTRINSIC TIMESCALE AND LONG-TERM INSTABILITY

In the main text, it was demonstrated that in the short-time regime, i.e., within 10^4 s, f_2 grows logarithmically. However, the eventual divergence of a log function implies that it has to breakdown at certain time point. Figure 5 confirms this. When the saturation of f_2 is taken into account, the overall fitting turns to favor an exponential curve, $a \exp(-bt) + c$. In

contrast to the scale-free logarithm, the intrinsic timescale $1/b$ reveals an interesting physics. Namely, the fluctuation of b in Fig. 10 is found to increase by more than three folds when θ is near either the phase boundary [the green solid line in Fig. 3(a), below which the ladder will slip] or θ_c [the blue dotted line across which the solution switches from Eqs. (4) and (5)]. Of course, we do not expect this finite and nonthermal system to exhibit a diverging correlation time-harbinger to a continuous phase transition. But the enhancement of $1/b$ near the phase boundary must be an integral part to the future theory for this macroscopically static and yet mesoscopically dynamic phenomenon.

We notice a common feature in Fig. 4 that we do not yet understand. Namely, upon reaching the upper limit f_2 will fluctuate for several hours before a precipitous drop. Simultaneously, the contact area begins to fluctuate vehemently to the point it appears discontinuous at times, as shown in Fig. 11.

-
- [1] D. Halliday, Robert Resnick, and J. Walker, *Fundamentals of Physics*, 10th ed. (Wiley, New York, 2013), p. 311.
 - [2] K. K. Hkkinen, J. Pesonen, and E. Rajamki, *J. Occupat. Accidents* **10**, 1 (1988).
 - [3] W.-R. Chang, C.-C. Chang, S. Matz, and D. H. Son, *Safety Sci.* **42**, 791 (2004).
 - [4] J. L. Synge and B. A. Griffith, *Principles of Mechanics* (McGraw-Hill, New York, 1959), pp. 82-86.
 - [5] E. C. Pestel and W. T. Thomson, *Statics* (McGraw-Hill, New York, 1969), pp. 247-248.
 - [6] K. S. Mendelson, *Am. J. Phys.* **63**, 148 (1995).
 - [7] J. Bennett and A. Mauney, *Phys. Teach.* **49**, 567 (2011).
 - [8] M. P. Silverman, *World J. Mech.* **8**, 311 (2018).
 - [9] Y. Salu, *Phys. Teach.* **49**, 289 (2011).
 - [10] A. G. Gonzalez and J. Gratton, *Am. J. Phys.* **64**, 1001 (1996).
 - [11] Video of our experiments can be found in <https://youtu.be/bW6ctucMrFg>.
 - [12] D. Kaplan, *Phys. Teach.* **51**, 224 (2013).
 - [13] T. S. Majmudar and R. P. Behringer, *Nature (Lond.)* **435**, 1079 (2005).
 - [14] K. E. Daniels, J. E. Kollmer, and J. G. Puckett, *Rev. Sci. Instrum.* **88**, 051808 (2017).
 - [15] F. P. Bowden and D. Tabor, *The Friction and Lubrication of Solids* (Clarendon, Oxford, 1950).
 - [16] P. Berthoud, T. Baumberger, C. Gsell, and J.-M. Hiver, *Phys. Rev. B* **59**, 14313 (1999).
 - [17] T. Baumberger and C. Caroli, *Adv. Phys.* **55**, 279 (2006).
 - [18] R. T. Spurr, *Br. J. Appl. Phys.* **6**, 402 (1955).
 - [19] C. A. Brockley and H. R. Davis, *J. Lubr. Technol.* **90**, 35 (1968).
 - [20] C. H. Scholtz and J. T. Engelder, *Int. J. Rock Mech. Min. Sci. Geomech. Abstr.* **13**, 149 (1976).
 - [21] J. H. Dieterich, *Pure Appl. Geophys.* **116**, 790 (1978).
 - [22] P. Berthoud and T. Baumberger, *Europhys. Lett.* **41**, 617 (1998).
 - [23] M. W. Pascoe and D. Tabor, *Proc. R. Soc. Lond. Ser. A* **235**, 210 (1956).
 - [24] J. H. Dieterich and B. D. Kilgore, *Pure Appl. Geophys.* **143**, 283 (1994).
 - [25] O. Ben-David, S. M. Rubinstein, and J. Fineberg, *Nature (Lond.)* **463**, 76 (2010).
 - [26] M. Watanabe, M. Karasawa, and K. Matsubara, *Wear* **12**, 185 (1968).
 - [27] S. M. Rubinstein, G. Cohen, and J. Fineberg, *J. Phys. D: Appl. Phys.* **42**, 214016 (2009).
 - [28] T. Pilvelait, S. Dillavou, and S. M. Rubinstein, *Phys. Rev. Research* **2**, 012056(R) (2020).
 - [29] S. Dillavou and S. M. Rubinstein, *Phys. Rev. Lett.* **124**, 085502 (2020).
 - [30] S. Mahajan, M. Tennenbaum, S. N. Pathak, D. Baxter, X. Fan, P. Padilla, C. Anderson, A. Fernandez-Nieves, and M. P. Pica Ciamarra, *Phys. Rev. Lett.* **124**, 128002 (2020).
 - [31] L. Vanel and E. Clément, *Eur. Phys. J. B* **11**, 525 (1999).
 - [32] I. Bratberg, K. Maloy, and A. Hansen, *Eur. Phys. J. E* **18**, 245 (2005).